Combustion and Flame 258 (2023) 112457

Contents lists available at ScienceDirect

Combustion and Flame

journal homepage: www.elsevier.com/locate/combustflame

Production of Aliphatic-Linked Polycyclic Hydrocarbons during Radical-Driven Particle Formation from Propyne and Propene Pyrolysis

James A. Rundel[a], K. Olof Johansson[b,c], Paul E. Schrader[b], Ray P. Bambha[b], Kevin R. Wilson[d], Judit Zádor[b], G. Barney Ellison[e], Hope A. Michelsen[a,b,f,*]

[a] Department of Mechanical Engineering, University of Colorado Boulder, 1111 Engineering Drive, Boulder, CO, 80309, USA
[b] Combustion Research Facility, Sandia National Laboratories, 7011 East Avenue, Livermore, CA, 94550, USA
[c] Presently at KLA Corporation, Milpitas, CA, 95035, USA
[d] Chemical Sciences Division, Lawrence Berkeley National Laboratory, Berkeley, CA, 94720, USA
[e] Department of Chemistry, University of Colorado Boulder, Cristol Chemistry, Boulder, CO, 80309, USA
[f] Environmental Engineering Program, University of Colorado Boulder, 1111 Engineering Drive, Boulder, CO, 80309, USA

ARTICLE INFO

Article history:
Received 1 June 2022
Revised 14 October 2022
Accepted 14 October 2022
Available online 4 November 2022

Keywords:
Pyrolysis
Propyne
Propene
Resonance-stabilized radicals
PAH

ABSTRACT

We investigated the pyrolysis of propyne and propene using aerosol mass spectrometry coupled with tunable synchrotron vacuum ultraviolet photoionization. The results show that propyne forms particles at pyrolysis temperatures approximately 100 K below the lowest temperature at which propene produces particles. The aerosol mass spectra show that the carbon-to-hydrogen (C/H) ratios of the pyrolysis products from both reactants increase with temperature between the particle onset temperature and 1275 K. In this temperature range, the mass peaks corresponding to species with 18 or more carbon atoms are more saturated (i.e., have lower C/H ratios) than species predicted by the stabilomer grid. The observation of relatively high saturation (low C/H ratios) at temperatures near particle onset is consistent with the presence of aliphatically linked hydrocarbons during the preliminary stages of soot formation. The masses of the species presumed to be aliphatically linked suggest that these linked species are adducts of species smaller than chrysene ($C_{18}H_{12}$). We performed a comparative analysis of the initial PAH-growth pathways consistent with aerosol mass spectra and associated mass-specific photoionization-efficiency curves. The results from the comparative analysis indicate that the development of PAHs up to the size of acenaphthylene ($C_{12}H_8$) follow similar formation pathways for propyne and propene, but the isomeric composition of species larger than acenaphthylene diverges for the two reactants.

1. Introduction

Soot is formed during incomplete combustion and pyrolysis of carbon-based fuels, such as fossil fuels and biomass. Anthropogenic burning of hydrocarbons in the industrial and transportation sectors is a primary contributor to soot emissions [1,2]. The widespread use of hydrocarbon fuels and the growing occurrence of large wildfires has led to increased bioavailability of polycyclic aromatic hydrocarbons (PAHs) in soil and water [2]. Several of these PAHs are known carcinogens or have been labeled as priority pollutants by the EPA [3,4]. Soot and combustion-generated particulates span a wide range of sizes, from ultrafine particles that can pass from the lungs into the bloodstream, to larger particles that can become trapped in the lungs. As a result, these particles have been linked to a wide array of negative health effects, including respiratory disease, altered cardiac function, and increased risk of death [5,6].

Soot emissions also have a significant negative impact on climate and air quality. Once emitted, soot particles can undergo physical and chemical aging processes, including interactions with other pollutants, such as ozone, sulfur and nitrogen oxides, and nitric acid, to further contribute to air pollution [7–9]. Soot contributes to global warming by directly affecting the global radiation budget as a result of its strong absorption in the ultraviolet, visible, and infrared wavelengths [1,8,10], and by indirect effects including altered surface albedo for snow and ice and cloud and ice particle nucleation [1,7,10,11].

* Corresponding author at: University of Colorado Boulder, Department of Mechanical Engineering, 1111 Engineering Drive, Boulder, CO, 80309, United States.
E-mail address: hope.michelsen@colorado.edu (H.A. Michelsen).

https://doi.org/10.1016/j.combustflame.2022.112457

These detrimental effects on human health and the environment have led to increased regulation, with an emphasis on emissions from internal combustion engines and power generation [12,13]. The ability to substantially reduce the formation of soot particles could have a profound effect on combustion and energy efficiency [10,12], public health [5,6,9], and the environment [1,7-11], and could facilitate meeting strict regulations on fine particle emissions. A more complete understanding of particle formation may enable the development of new fuels and control schemes to reduce or manage soot production. The ability to control soot emissions is hindered, however, by an incomplete understanding of particle formation.

The chemistry associated with soot formation may also be important for the commercial production of carbonaceous materials, such as carbon black, graphite, graphene, and carbon nanotubes [14–16]. Developing a better understanding of the chemical mechanisms involved may provide more efficient routes to the synthesis and design of novel materials.

PAHs have long been associated with soot formation [17–19] and are accepted as gas-phase precursors to soot. Numerous mechanisms have been proposed to explain the growth of PAHs; the most widely studied, validated, and invoked of these mechanisms is the hydrogen-abstraction-C_2H_2-addition (HACA) mechanism [20]. Connecting PAH growth to particle formation, however, has proven to be more challenging, and the mechanisms driving particle inception, the transition from gas-phase precursors to condensed-phase particles [21], have not yet been definitively identified.

Johansson et al. [22] recently proposed an inception mechanism involving chain reactions driven by resonance-stabilized radicals (RSRs). This mechanism, dubbed the clustering-of-hydrocarbons-by-radical-chain-reactions (CHRCR) mechanism, is based on experimental observations of RSRs formed under a wide range of flame conditions and fuels and theoretical investigations demonstrating the feasibility of the mechanism. The RSRs observed by Johansson et al. [22] had been observed previously in soot extracted from flames [23–28] and had been shown to be readily formed through reactions of RSRs with the common combustion byproduct acetylene [29,30]. Jin et al. [31–33] and Couch et al. [34] have shown that reactions involving the RSRs propargyl, benzyl, vinylcyclopentadienyl, and indenyl participate in radical-chain reactions leading to molecular growth of PAHs at high temperatures. Rundel et al. [35] further demonstrated that reactions driven by indenyl facilitate particle formation during the pyrolysis of indene and ethylene seeded with a small amount of indene. These experiments yielded a significantly lower particle-formation temperature for indene pyrolysis than for ethylene pyrolysis and a similar onset temperature for indene-seeded ethylene as for indene pyrolysis alone.

Small C_3 hydrocarbons, such as propyne and propene, are important intermediates in combustion processes as they are formed during both the decomposition of larger fuels and molecular-weight growth from C_1–C_2 fuels [36–38]; they are thus often abundant during combustion and pyrolysis processes. The loss of a hydrogen atom leads to propargyl formation from propyne, the barrier for which is 90.1 kcal/mol [39,40], as shown in Scheme 1. Likewise, allyl is produced by the removal of a hydrogen atom from propene with a barrier of 85.8 kcal/mol [41] (also shown in Scheme 1). Propargyl and allyl are among the smallest and most common RSRs. These two RSRs have been recognized as important intermediates leading to the production of the “first aromatic ring” through combination reactions [42,43]. Because the first aromatic ring is often regarded as a critical and rate-controlling step in PAH and soot formation [44,45], a significant body of work has been developed around the kinetics for reactions involving propyne/propargyl [42,43,46,47] and propene/allyl [48–51].

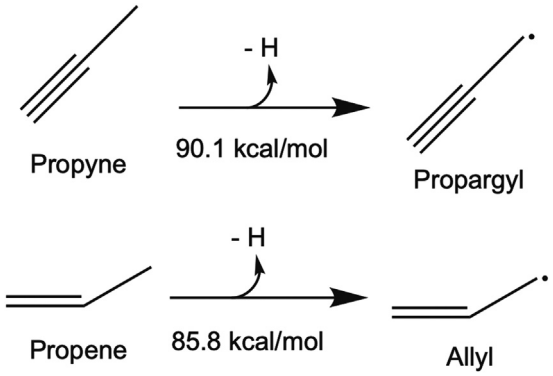

Scheme 1. Formation of propargyl and allyl radicals from propyne and propene.

However, much of this work has been limited to the examination and modeling of species with six carbon atoms (C_6) or smaller.

More recently, investigations of propyne and propene pyrolysis and combustion have expanded to examine the formation and growth of larger PAHs beyond the first aromatic ring [52–58]. These investigations have largely focused on investigating multi-ring PAH concentrations in the gas phase and assessing the performance of kinetic mechanisms in predicting PAH formation, focusing on reactions involving C_3 species. In these works, studies of detailed reaction pathways and kinetic modeling considering PAH growth have generally focused on species smaller than C_{16} or four fused rings. Despite the extensive body of literature on the kinetics of high-temperature hydrocarbon chemistry, there have been few studies on the development of PAHs larger than pyrene ($C_{16}H_{10}$) under combustion and pyrolysis conditions. There is also a poor understanding of the role of allyl and propargyl radicals in soot inception and growth.

In this paper, we describe experiments designed to identify the role of allyl and propargyl on particle formation during pyrolysis. We pyrolyzed argon-diluted propyne and propene in a flow reactor at 1 atm and temperatures between 973 and 1573 K, leading to the formation of carbonaceous particles. The development of particles and associated products was studied using aerosol mass spectrometry coupled with tunable vacuum-ultraviolet (VUV) radiation. Tunable VUV radiation allowed for an investigation into isomeric compositions of pyrolysis products using mass-specific photoionization efficiency (PIE) curves, with which products of the pyrolysis of the two reactants were compared. The objectives of this study were (1) to provide molecular-level insight into the pathways and species relevant to precursor growth and soot inception and growth in propyne and propene pyrolysis and (2) to investigate the role(s) of propargyl and allyl as the smallest and most common RSRs in soot formation, especially in relation to the CHRCR mechanism. The high degree of overlap in decomposition products between propyne and propene [53] allows for a comparative analysis of how the propargyl and allyl radicals may influence the formation of larger precursors and the dependence of growth pathways on the reactant structure.

2. Experimental and analysis methods

2.1. Experimental setup

Pyrolysis experiments were performed at Beamline 9.0.2 at the Advanced Light Source (ALS) synchrotron facility at Lawrence Berkeley National Laboratory (LBNL) in Berkeley, CA. The experimental setup has been described previously [35], and only a brief overview is given here. The pyrolysis setup uses a laminar flow reactor made of a quartz tube heated by an electric furnace

(MHI-H17HTC). The reactor has an inner diameter of 1.08 cm, and the heated length is 40.6 cm. The reactor was operated under ambient conditions at the ALS with a nominal working pressure of 1 atm. Pyrolysis products were analyzed using a time-of-flight aerosol mass spectrometer coupled with synchrotron tunable vacuum ultraviolet photoionization (VUV-AMS) [59,60].

Propyne ($CH_3C{\equiv}CH$) and propene ($CH_3CH{=}CH_2$) were pyrolyzed at temperatures between 973 and 1573 K, inclusive. Within this temperature range, particles were generated from both reactants. Flows of 5 sccm of reactant and 200 sccm of argon were supplied to the reactor inlet; this mixture corresponds to a reactant concentration that is 2.4% of the total by number density. Assuming a uniform temperature distribution within the heated portion of the reactor at 973 K yields an estimated minimum residence time of approximately 3.1 s. At the exit of the reactor, pyrolysis products were diluted with a 3000 sccm flow of nitrogen and continuously sampled by the VUV-AMS. The VUV-AMS incorporates an aerodynamic lens (ADL) system [61–63], which focuses particles with an aerodynamic diameter larger than approximately 50 nm into a beam and removes particles and gas-phase species below this threshold. During the sampling process, smaller particles coagulate and form particles large enough to be transmitted through the ADL system to the detection region. The particle beam impinges on a heated copper target (623 K for these experiments), which vaporizes condensed and weakly bound species from the particles. The vaporized species are photoionized with VUV radiation and analyzed with time-of-flight (TOF) mass spectrometry.

We typically recorded mass spectra using a photon energy of 9.5 eV, which can ionize most products within our detection range (greater than approximately 40 u) with limited fragmentation. We assumed the species detected were singly ionized. The resolution of the TOF mass spectrometer ($m/\Delta m$) is approximately 1600 at m/z 230, which is sufficient to resolve mass peaks separated by a single H atom (1 u). The energy spread of the VUV beam was approximately 0.2 eV FWHM. We measured mass spectra as a function of photon energy over the range of 7.5 – 10.2 eV. These measurements provided a measure of the photoionization efficiency of species at selected masses. We introduced a small amount of 2,5-dimethylfuran (m/z 96) into the detection region to serve as a measure of photon flux for these photoionization efficiency measurements. The 2,5-dimethylfuran peak was also useful for mass calibration.

In these experiments, species concentrations are not readily quantifiable from the VUV-AMS signal intensity because of complex interactions between available species and particles [22,35]. The VUV-AMS measures species that are bound strongly enough to the particles to transit to the ionization chamber but are bound weakly enough to vaporize from the particle at the heated target. This process tends to provide relatively high sensitivity to heavier masses and certain radicals [22].

2.2. Analysis methods

Photoionization efficiency (PIE) curves were produced for selected mass peaks to provide insight into their isomeric composition. The PIE curves span photon energies between 7.5 and 10.2 eV with a sampling resolution of 0.1 eV. Integrated peak areas used to produce PIE curves were obtained by fitting the experimental peaks to a baseline-corrected functional form of a gaussian or exponentially modified gaussian in Igor Pro (Version 8.04 [64]). The experimental PIE curves were corrected for photon flux based on the response of the 2,5-dimethylfuran peak and the known photoionization cross-section published by Xie et al. [65].

We compared PIE curves from propyne with those from propene to provide a semi-quantitative analysis of the isomeric composition for a given mass peak between the two reactants. For these comparisons, both PIE curves were normalized by their maximum signal; then one PIE curve was vertically scaled to provide the best fit between the two curves. The quality of the fit between PIE curves for the two reactants was assessed using the chi-squared value for the fit, which decreases with increasing curve similarity. We also made comparisons between the PIE curves of the pyrolysis products and reference curves available in the literature. Overall fits between our experimental PIE curves, $\mathrm{PIE_{fit}}(\nu)$, and multiple reference curves, $\mathrm{PIE_i}(\nu)$, were computed based on a linear combination of reference curves convolved with the photon-energy distribution, $G(\nu)$, at 9 eV. These fits were calculated as

$$\mathrm{PIE_{fit}}(\nu) = \sum_i a_i (G * \mathrm{PIE}_i)(\nu) + b \quad (1)$$

where a and b are scaling factors, i is an index denoting different isomers, and ν is the photon energy. The scaling factor b represents an initial offset and was only used when there was a non-zero signal for both the experimental and reference PIE curves at our initial scan energy of 7.5 eV.

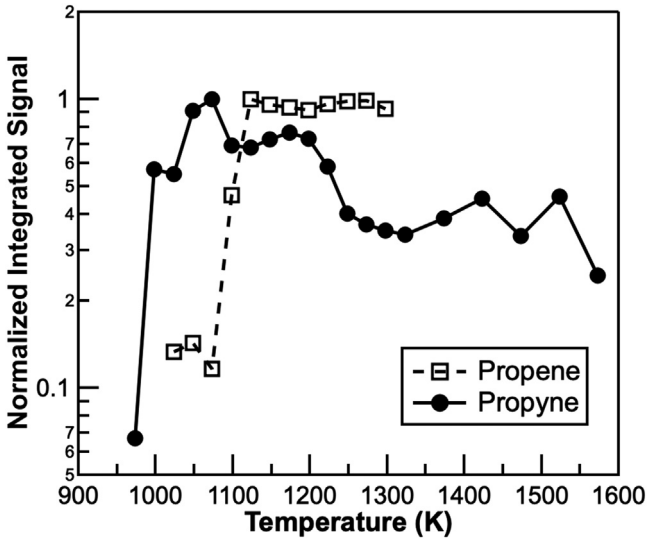

Fig. 1. Temperature dependence of the normalized, integrated VUV-AMS signal. VUV-AMS mass spectra were integrated over the m/z range of 50–600, normalized to unity at the integrated maximum, and plotted as a function of the flow-reactor temperature. Results are shown for the pyrolysis of propene (open squares) and propyne (circles).

3. Results and discussion

3.1. Soot onset temperature

Because the VUV-AMS yields significant signal only when particles are sampled, the temperature-dependent propensity for particle formation can be inferred from the VUV-AMS ion signal integrated over the range of m/z measured at each temperature [35]. Because the transmission of small particles is limited by the ADL system, the onset temperatures for particle formation derived from the VUV-AMS measurements may be slightly higher than those yielded by measurements more sensitive to particles smaller than 50 nm, as suggested by previous comparisons with complementary mobility size measurements [35]. Under our conditions, however, coagulation facilitates detection of small particles, and thus this technique provides a consistent standard for comparison. Fig. 1 shows a comparison of the integrated VUV-AMS signal as a function of temperature for the pyrolysis experiments. There is a difference of 100 K in particle-onset temperature between propyne and propene; propyne forms particles at a lower temperature than

propene. The integrated signal indicates that particle formation begins between 975 and 1000 K for propyne and between 1075 and 1100 K for propene.

Previous similar measurements demonstrated particle-onset temperatures in the range of 1148–1173 K for ethylene pyrolysis and 1023–1033 K for indene pyrolysis, based on integrated VUV-AMS ion signals [35]. For the ethylene measurements, the estimated residence time (3.1 s at 973 K) and concentration (2.4% of the total by number density) were the same as for the propyne and propene experiments described here. For indene, the estimated residence time of 2.5 s was shorter, and the concentration was significantly lower (0.04% of the total by number density). Nevertheless, the low onset temperatures for propyne, propene, and indene, compared to that of ethylene, indicate that the products produced during the pyrolysis of these reactants facilitate a more efficient pathway to particle formation. In this paper, we focus on the differences between propyne and propene pyrolysis.

As shown in Fig. 1, propyne forms particles at lower temperatures than propene. Previous flow-reactor studies have shown that propyne is produced by propene pyrolysis at temperatures above 950–1000 K at a pressure of 80 kPa with a residence time of 2.4 s [56]. At a similar pressure (approximately 100 kPa) and residence time (3.1 s), our measurements demonstrate a particle-onset temperature range for propene of 1075–1100 K. The higher soot onset temperature for propene compared to propyne pyrolysis indicates that the formation of propyne from propene is not sufficiently fast at temperatures near the propyne onset temperature (975–1000 K) to drive particle formation at these temperatures, despite the more energetically favorable formation of the allyl radical from propene than the propargyl radical from propyne [39,41].

The self-reaction of propargyl radicals is likely an active pathway in the initial stages of propyne pyrolysis because of the high concentration of propargyl radicals. This reaction has been well documented as an important route to the formation of benzene, the first aromatic ring [42,66-68], which is thought to serve as a critical step in the formation of PAHs. Recent work details the discovery of a pathway in the isomerization of fulvene to benzene with a lower barrier than suggested by previous theoretical studies [68]. This discovery demonstrates the potential for improvements in the understanding of the C_6H_6 potential energy surface (PES). A thorough understanding of the C_6H_6 PES and important chemical pathways and intermediates in propargyl recombination may provide further insight into the role of associated reactions on particle formation. This information is also relevant to soot modeling and chemical kinetic mechanisms, which often oversimplify this chemistry to focus on the formation of fulvene and benzene.

Previous studies have found that propyne and propene both begin to produce benzene at comparable temperatures in a pyrolytic environment [47,49,51,69]. Both reactants also produce allyl and propargyl radicals, and reactions between allyl radicals or allyl + propargyl reactions have been shown to lead to products with 5- and 6-membered rings [46,70-72]. Despite these similarities, propyne and propene do not start forming particles at the same temperature. The difference in particle-onset temperatures between the two reactants indicates that, although the formation of the 'first ring' is an important step toward the formation of PAHs, it does not account for the temperature dependence of particle formation under our experimental conditions; initial particle formation must thus be driven by other factors. Small radicals, such as allyl and propargyl, play an important role in the formation and growth of aromatics and, following the CHRCR mechanism, one might expect both allyl and propargyl to participate in radical addition reactions to form larger RSRs or serve as initiators for hydrocarbon clustering. However, the difference in particle onset temperature suggests that the structure or kinetics of the species associated with RSRs and their adducts may also play an important role in the early stages of particle formation.

3.2. Temperature dependence of large PAHs

Despite recent work that examined gas-phase molecular-weight growth in propyne and propene systems [52,53,55,58], information on the development of species larger than C_{12}–C_{14} in these systems is scarce. The experimental work in this study is complementary to prior gas-phase work as the VUV-AMS data emphasize species larger than approximately C_{12} and products associated with particles. This section examines the relationship between pyrolysis temperatures and the development of species larger than *m/z* 160, with an emphasis on how these findings relate to soot inception and growth.

3.2.1. Propyne pyrolysis

Fig. 2 shows VUV-AMS mass spectra for propyne pyrolysis at three temperatures. These mass spectra demonstrate that the number of hydrogen atoms for a given number of carbon atoms is strongly temperature dependent. At the onset temperature of 1000 K (Fig. 2a), when particles are first detected by the VUV-AMS, there is a relatively large distribution of mass peaks within a given peak series (clusters of peaks associated with a selected number of carbon atoms), and prominent peak series are seen for species with both even and odd numbers of carbons. The range of peaks within each peak series corresponds to different numbers of hydrogen atoms (i.e., levels of saturation) for the associated number of carbons. For species larger than C_{16}, many of the prominent mass peaks do not have masses that correspond to stable peri–condensed PAHs at the onset temperature. As temperature increases, the saturation level of a given peak series decreases, and the peaks within a series converge to masses associated with peri–condensed PAHs.

Such masses, particularly those with even numbers of carbon atoms, are often assumed to correspond to those of the most thermodynamically stable species, i.e., stabilomers, identified by Stein and Fahr [73]. Numerous studies have shown, however, that the isomers associated with masses such as *m/z* 178, 202, 226, 228, 250, and 300 observed during high-temperature particle formation are frequently non-stabilomers isomers [35,67,74-77]. Nevertheless, the stabilomer grid is a convenient point of reference for the elemental composition of the least saturated peri–condensed PAH expected for a given number of carbons. According to the stabilomer grid, for example, the peak cluster associated with C_{22} species would be expected to have prominent peaks at *m/z* 274 ($C_{22}H_{10}$) and 276 ($C_{22}H_{12}$). However, at 1000 K, the prominent peaks associated with C_{22} species in the experimental mass spectrum shown in Fig. 2a are in the range of *m/z* 278–284 ($C_{22}H_{14}$ - $C_{22}H_{20}$), which corresponds to a difference of as much as 8 u above the stabilomer masses for C_{22} species. The species observed tend to have more hydrogen and thus a lower carbon-to-hydrogen ratio (1.10 – 1.57) than those of the stabilomers for C_{22} species (1.57–2.20).

The density of peaks observed in the mass spectra shows a strong dependence on the pyrolysis temperature. As temperature increases, the overall number of peaks decreases significantly. During this process, the relative intensity of odd-carbon peaks, which have been previously linked to structures containing cyclopenta moieties and resonance-stabilized radicals [22,32,74], decreases dramatically and disproportionately relative to the even-carbon peaks. The reduction in observed peaks occurs at temperatures within approximately 100 K above the particle-onset temperature as determined by the VUV-AMS signal (Fig. 2a-b). At higher temperatures, the mass spectra converge to an abbreviated set of peaks shown in Fig. 2c. This higher temperature mass spectrum (i.e., Fig. 2c) contains primarily even-numbered carbon series with

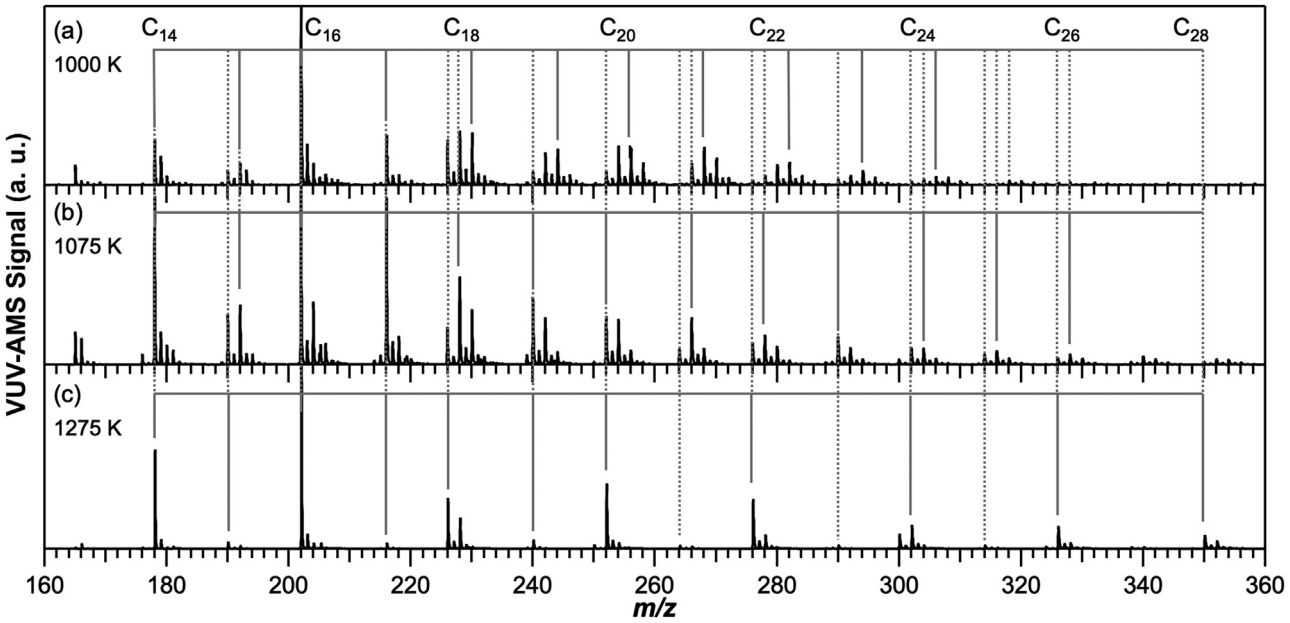

Fig. 2. VUV-AMS mass spectra from propyne pyrolysis at selected flow-reactor temperatures. Mass spectra were recorded at 9.5 eV and temperatures of (a) 1000 K, (b) 1075 K, and (c) 1275 K. Solid vertical lines indicate the largest peak in a series, and dotted lines highlight a constant mass between the mass spectra.

only 1–2 prominent peaks per carbon number, and the masses of these peaks correspond to those of the stabilomer PAHs. More highly saturated species are observed in the VUV-AMS mass spectra close to the particle-onset temperature, and species with significantly larger C/H ratios are observed at higher temperatures.

The large number of mass peaks and higher saturation of species, particularly large species ($>C_{17}$), are not explained by thermodynamic arguments alone, e.g., based on the stabilomer grid. These observations of large species with low C/H ratios are also inconsistent with mechanisms predicting continued sequential growth and subsequent cyclization of the preceding reactants, such as those typically invoked by HACA. Rather, the high hydrogen content of these large species is inconsistent with peri–condensed PAHs with primarily sp^2 hybridization and indicates products with aliphatic content. Such products would be expected from radical-driven clustering reactions, possibly involving propargyl. These products are likely to include structures such as aliphatically bridged and linked PAHs and PAHs with aliphatic sidechains and substitutions. These findings are consistent with the aliphatically linked PAH structures initially proposed by D'Anna et al. [78] and Dobbins and Subramaniasivam [79] and the significant aliphatic content associated with incipient particles observed by Wang and coworkers [26,80]. Frenklach [81] proposed that aliphatically linked PAH clusters would be more likely to form under conditions in which particle fragmentation does not readily occur.

The results support theories suggesting a route to soot inception through the formation of covalently bound clusters. Furthermore, the evidence of high levels of saturation for series larger than C_{17} indicates that the associated structures are primarily composed of covalently bound clusters of smaller species, such as those predicted by the CHRCR mechanism. In contrast to nucleation of physically bound clusters, barriers for the forward reactions of the CHRCR mechanism are expected to be much smaller than barriers for the reverse reactions at the temperatures for which we observe particle inception [22]. At these temperatures, chain-termination steps associated with the CHRCR mechanism are likely to produce relatively stable (even carbon) PAHs following rearrangement; this rearrangement may proceed at temperatures slightly higher than onset temperatures. Our data demonstrate that this route to molecular-weight growth occurs in the absence of acetylene and thus explains the formation of such PAHs without the need to invoke the HACA mechanism.

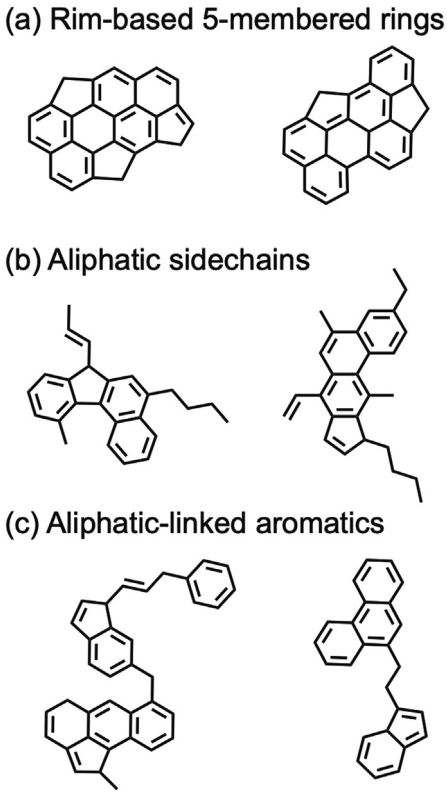

Fig. 3. Conceivable structures for species produced by clustering-type reactions. The species shown are representative of classes of structures that could be produced by mechanisms involving chemical clustering, such as the CHRCR mechanism.

There are a couple of explanations for these observations, which can be linked to the presence of various molecular structures, summarized in Fig. 3. One possibility is that these more saturated species are peri–condensed PAHs with multiple 5-membered rings,

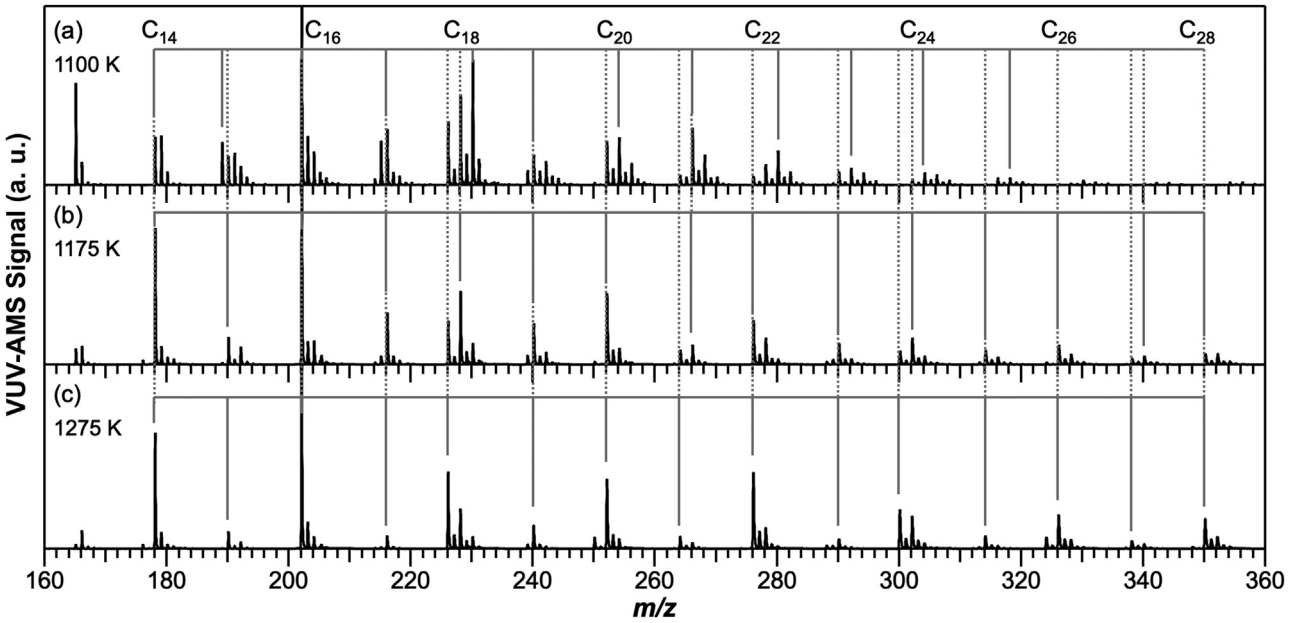

Fig. 4. VUV-AMS mass spectra from propene pyrolysis at selected flow-reactor temperatures. Mass spectra were recorded at 9.5 eV and temperatures of (a) 1100 K, (b) 1175 K, and (c) 1275 K. Solid vertical lines indicate the largest peak in a series, and dotted vertical lines highlight a constant mass between mass spectra.

each of which can have an sp^3 hybridized carbon if they occur at the outer edge of the molecular structure. Species with rim-based 5-membered rings were proposed to be important in the CHRCR mechanism because they can readily form an RSR, which can lead to further clustering [22]. Such species have been observed to be associated with soot inception [82,83], and recent theoretical studies have supported this hypothesis [84–86].

A second possibility involves aliphatic sidechains on substituted peri–condensed PAHs. Such species have been hypothesized to participate in the early stages of soot formation and lead to enhanced particle nucleation rates [26,80,87]. Recently, PAHs with aliphatic substitutions and sidechains were directly observed in young soot particles via atomic force microscopy [82,83]. Molecular dynamics simulations have hypothesized that aliphatic sidechains can facilitate physical dimerization of PAHs [87]. H-loss/addition on a sidechain could also lead to the formation of an RSR.

A related third possibility involves aliphatic-linked aromatic structures [78,79], which are also proposed to be produced during CHRCR-type clustering [22]. These structures are formed through chemical pathways that covalently link PAHs and can form three-dimensional polymer-like structures [88]. Experimental investigations have provided evidence for the presence of this type of molecular species adsorbed to incipient particles [78,79,82,83] and extracted from an inverse flame [89]; such structures may support multiple reactive sites and maintain an RSR-type character promoting further clustering and growth. Whereas these aliphatic-linked aromatic structures have been considered in molecular dynamics simulations [87,90], chemical reactions leading to this type of structure have not been incorporated into most kinetic models, limiting the ability to accurately model the inception process.

The increased levels of saturation observed for large species in the mass spectra for propyne pyrolysis are indicative of structures with increased aliphatic content, such as those shown in Fig. 3; however, the reaction rates involved in the formation of such species remain ambiguous. Prior work has provided evidence of the presence of a pool of RSRs in a flame and reactions that contribute to the development of this radical pool [22]. These RSRs have also been linked to rapid precursor growth and clustering reactions during particle formation and are capable of facilitating particle formation when added as a dopant at temperatures where the forward rates of HACA-type reactions are not favorable [35]. Johansson et al. [22] indicated that the forward reaction rates for the growth and clustering of RSRs could support particle formation and that the reverse rates for these reactions are small; however, continued work is needed to determine the rate coefficients associated with these reactions and incorporate them into kinetic models.

3.2.2. Propene pyrolysis

Despite the difference in particle onset temperature between propyne and propene, propene demonstrates the same temperature-dependent trends in peak density and C/H ratios observed for propyne. Fig. 4 shows the development of the mass spectra in propene pyrolysis with increasing temperature between the approximate particle-onset temperature (1100 K) and 1275 K. The implications of these trends, discussed in Section 3.2.1 with respect to propyne, are also applicable to propene. The large range of peaks indicating more saturated species for a given carbon number, particularly for species larger than C_{17}, suggests the presence of structures that may include multiple rim-based 5-membered rings with an sp^3 hybridized carbon, PAHs with aliphatic sidechains and substitutions, and/or aliphatic-linked aromatic structures.

At the onset temperature for propene, the range of peaks observed in the mass spectrum (Fig. 4a) for a specific number of carbons larger than C_{17} is approximately 2 u smaller than observed for propyne at the onset temperature (Fig. 2a). At comparable temperatures above 1150 K, however, there are negligible differences in the mass range of peaks for a given number of carbons between the two reactants. As with propyne, the saturation level for propene decreases dramatically with temperature between onset and 1275 K, particularly for species larger than C_{17}, as discussed in more detail in Section 3.2.3.

3.2.3. Carbon-to-hydrogen ratio

Fig. 5 shows the average carbon-to-hydrogen (C/H) ratio for each mass spectrum over selected mass ranges. The C/H ratio was calculated as the number of carbon atoms divided by the number of hydrogen atoms for each mass peak, corrected for contributions

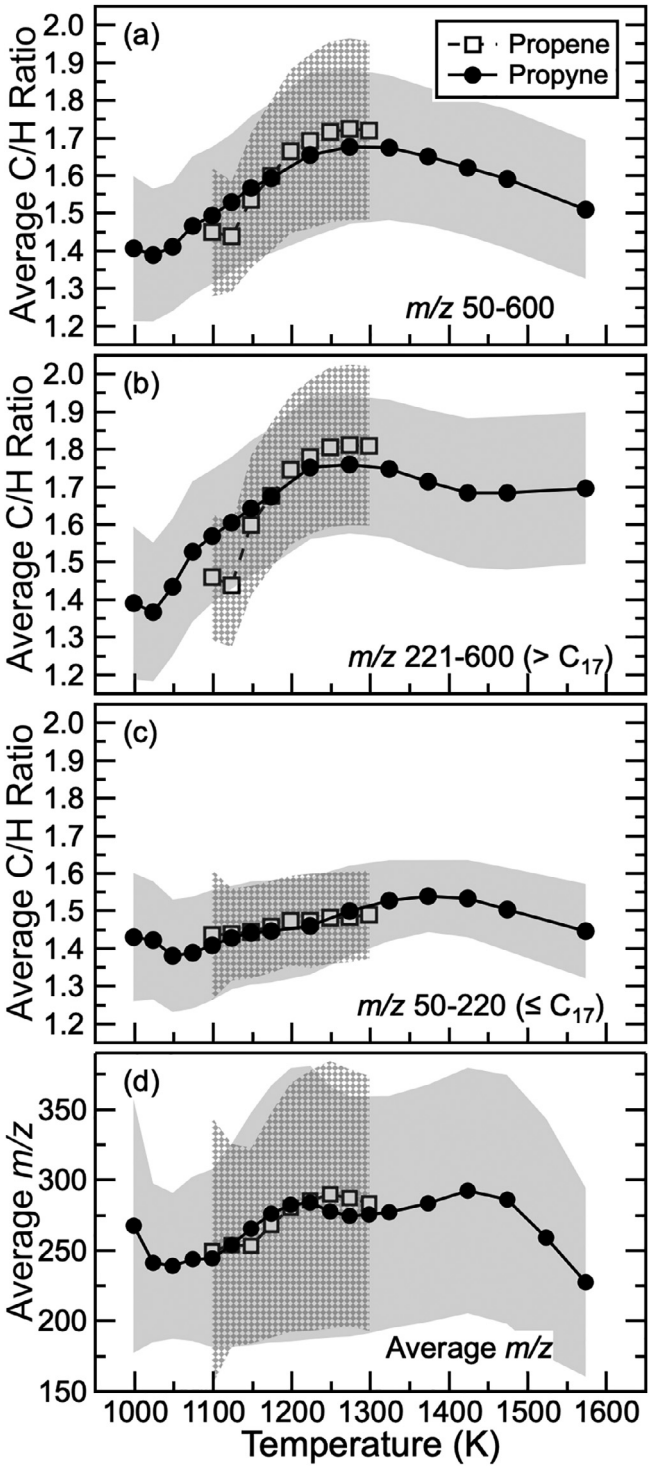

Fig. 5. Temperature dependence of the carbon-to-hydrogen (C/H) ratio and average mass from VUV-AMS mass spectra. C/H ratios are shown for portions of the mass spectrum averaged over (a) the full mass spectrum (*m/z* 50–600), (b) masses corresponding to C_{18} and larger species (*m/z* 221–600), and (c) masses corresponding to C_{17} and smaller species (*m/z* 50–220). Values were calculated on an atomic basis as a weighted average based on peak intensities. The average mass over the full mass spectrum (*m/z* 50–600) is shown in (d). The shaded regions represent one standard deviation of the mean.

from C_{13}, and weighted by the peak intensities. Peaks with intensities less than 1% of the largest peak were not included in the calculations.

Fig. 5a shows that the average C/H ratio from propyne and propene pyrolysis increases with increasing temperature for temperatures below 1275 K, as noted in Sections 3.2.1 and 3.2.2. The values are the same for propene and propyne within one standard deviation of the mean representing the spread of values at each temperature. Fig. 5b shows that the mean C/H ratio for species larger than C_{17} increases dramatically with increasing temperature, indicating a transition from species with higher levels of saturation and aliphatic character at lower temperatures to less saturated species with more aromatic character at higher temperatures. This increase in C/H ratio is correlated with an increase in the average mass of the species observed, as shown in Fig. 5d. This correlation is consistent with rearrangement and addition of aromatic rings as increasing temperature allows internal rearrangements to be energetically accessible. Fig. 5c shows that species the size of C_{17} and smaller maintain lower C/H ratios with increasing temperature and do not reach C/H ratios as large as those attained by the larger species.

At temperatures above approximately 1275 K, the C/H ratio plateaus or decreases (Figs. 5a-c). The average species mass demonstrates similar behavior (Fig. 5d). The range of masses observed for propyne remains relatively constant with increasing temperatures above 1275 K, but the largest peaks are at lower masses, shifting the average mass toward the low end of the mass range. At higher temperatures, the species observed in the mass spectra are smaller and primarily even-numbered carbon species with masses corresponding to stabilomers, as shown in Fig. 2. Although particles are likely still growing at these temperatures, species that attach to the particle surface may be more firmly bound by covalent bonds, preventing vaporization on the heated target and detection by the VUV-AMS.

Fig. 6 shows comparisons of the temperature dependence of the C/H ratio for selected series of mass peaks for propyne (Fig. 6a) and propene (Fig. 6b). The C/H ratios for peak series larger than C_{17} demonstrate a strong temperature dependence not observed for series at C_{17} and smaller, for both reactants. The C/H ratios for the C_{16} and C_{17} series are relatively constant with temperature, whereas the C/H ratios of the C_{21} and C_{22} series increase sharply within the first 100 K following soot onset and then reach a plateau with temperature above approximately 1275 K. Both odd- and even-numbered carbon series exhibit the same trends in each size regime. These trends suggest that the more saturated species apparent at temperatures near particle onset for C_{21} and C_{22} are likely formed through the clustering of smaller species.

Fig. 7 shows the dependence of the C/H ratio on the number of carbons for selected peak series at selected temperatures, compared to the C/H ratio of the associated stabilomer species. At temperatures near their respective particle onset temperatures, the C/H ratios for both propyne and propene are consistently lower than the C/H ratios of the stabilomers for species larger than C_{17}, whereas the C_{16} peak series is in better agreement with the C/H ratios for stabilomer species. The C_{18} series shows an intermediate trend with a slightly reduced C/H ratio, relative to the stabilomers, but the decrease in the C/H ratio is not as significant as for larger species. This trend is more pronounced for propene, which has a higher relative intensity for *m/z* 230 (C_{18}) at the particle onset temperature (Fig. 4a) than does propyne (Fig. 2a). As temperature increases, however, the even-numbered carbon series tend toward the C/H ratios of stabilomer masses associated with the given carbon number. The large difference in structure and composition between the observed species and the most thermodynamically stable species is consistent with the hypothesis that

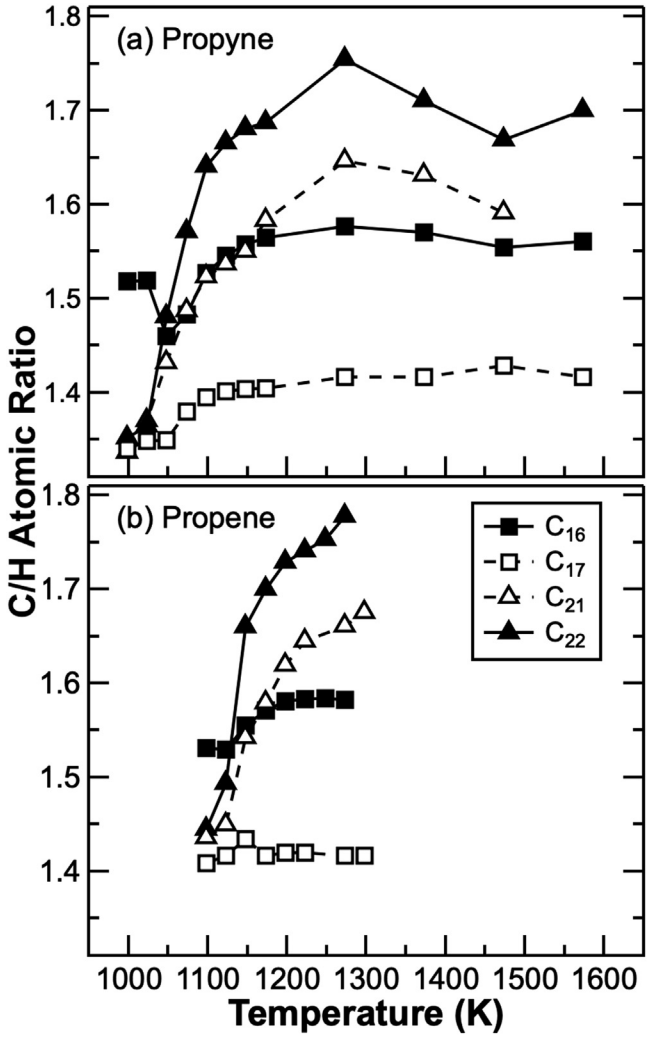

Fig. 6. Temperature dependence of the carbon-to-hydrogen (C/H) ratio of selected peak series. The series are associated with different numbers of carbon atoms. Values were calculated on an atomic basis as a weighted average based on peak intensities. Results are presented for peaks corresponding to the C_{16}, C_{17}, C_{21}, and C_{22} series (as indicated in the legend) for (a) propyne and (b) propene.

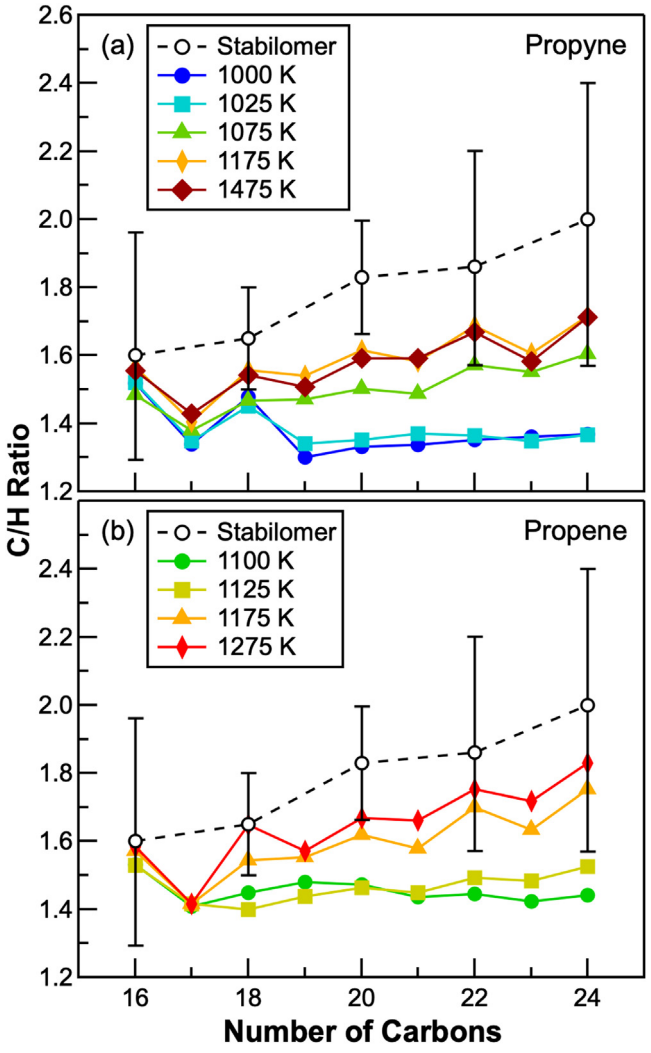

Fig. 7. Dependence of C/H ratio on the number of carbons for a given peak series. Results are shown for (a) propyne and (b) propene. Solid lines and symbols represent the C/H ratios of peak series for selected flow-reactor temperatures, as indicated in the legend, and the dotted line and open symbols show the average C/H ratio of stabilomers [73]. Error bars represent the range of C/H ratios for stabilomers with a given number of carbons.

covalent-clustering reactions play a prominent role in generating large species and new particles at inception temperatures.

In addition to the temperature dependence of the C/H ratios, Fig. 7 also demonstrates a trend in the relationship between the C/H ratio and odd/even-numbered carbon series. At intermediate and high temperatures, even-numbered carbon series (C_{2n}) display higher C/H ratios than the following odd-numbered carbon series (C_{2n+1}) at a higher mass. Prior work by Campbell et al. [91] and Desgroux et al. [28], which examined particles extracted from flames using particle mass spectrometry, also demonstrated the presence of large species containing both odd and even numbers of carbons with a relatively wide range of saturation levels. Contributions from oxygenated species were not fully resolved, however, and there were no discernable trends between odd- and even-numbered carbons and the C/H ratios for the respective peak clusters. The trend between odd- and even-numbered carbons and the C/H ratio shown in Fig. 7 suggests that, at intermediate and high temperatures, the even-numbered carbon series have high C/H ratios and significant aromatic content while the odd-numbered carbon species are more likely to contain features such as 5- or 7-membered rings and sidechains. At lower temperatures, however, the distinction in C/H ratios between odd- and even-numbered carbons is significantly diminished for large species, and both series show comparable levels of saturation, indicating decreased aromaticity in the even-numbered carbon series.

3.3. Comparative analysis of reaction networks

We conducted a comparative analysis of the pyrolysis products from propyne and propene, using the VUV-AMS mass spectra and PIE curves to develop a better understanding of the reaction pathways, products, intermediates, and potential effects linked to reactants and RSR structure. The initial masses observed in propyne pyrolysis are very similar to those produced in propene pyrolysis, suggesting a high degree of overlap in products and growth pathways for the two reactants. This analysis is used to outline a contextual reaction network, focusing on the initial growth pathways, and to investigate the major isomeric components of selected mass peaks. We focused on hydrocarbon-based reactions in a pyrolytic environment; however, previous VUV-AMS analysis of soot particles extracted from a premixed ethylene flame revealed the presence of large oxygenated species [92], which may be relevant to growth pathways in an oxidative environment.

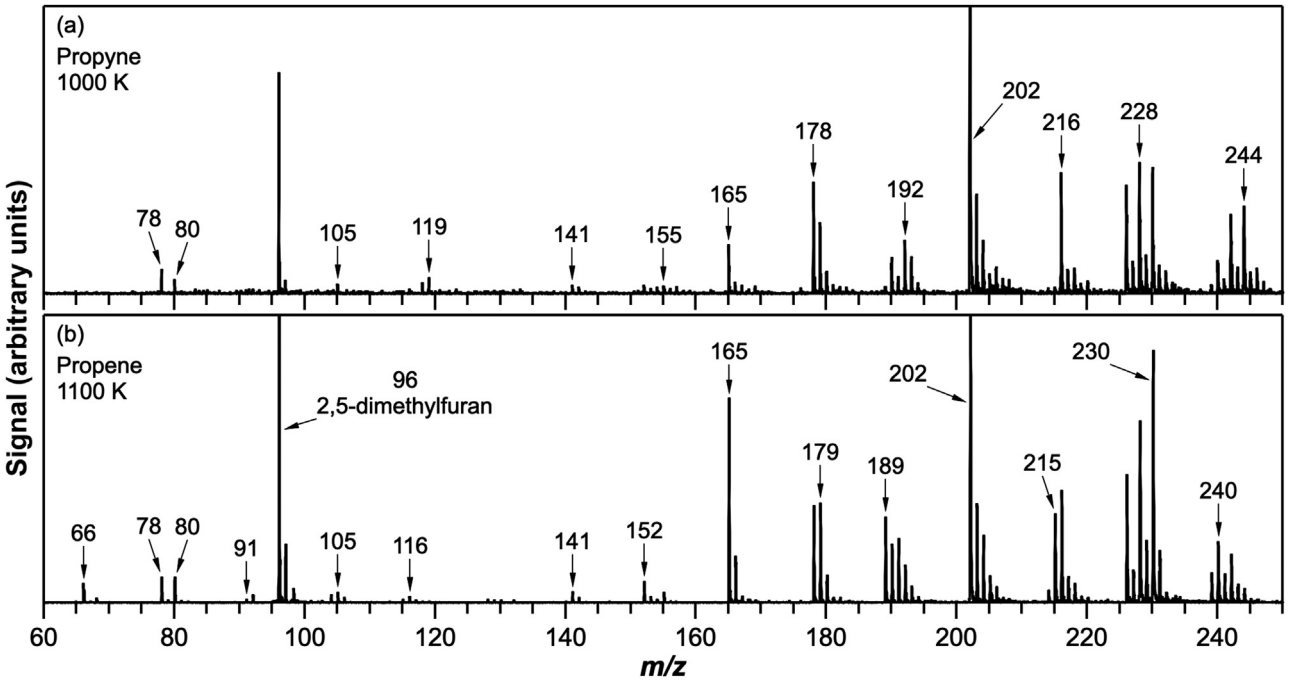

Fig. 8. Comparison of VUV-AMS mass spectra at the particle-onset temperature. Mass spectra are shown for (a) propyne at a flow-reactor temperature of 1000 K and (b) propene at a temperature of 1100 K over the mass range of *m/z* 60–250. The VUV-AMS mass spectra were recorded at a photon energy of 9.5 eV.

3.3.1. Initial growth pathways

Fig. 8 shows VUV-AMS mass spectra for the two reactants at their respective soot onset temperatures. The large peak in both mass spectra at *m/z* 96 corresponds to 2,5-dimethylfuran, which was injected into the ionization chamber as a reference and was not present in the flow reactor. The mass spectra for both reactants demonstrate prominent peaks in the range of C_5–C_9 species, which is somewhat unexpected, considering that the VUV-AMS has a lower sensitivity to masses in this range. Their appearance in the mass spectra underscores their involvement during the early stages of particle formation and growth. Scheme 2 presents a summary of potential growth pathways for species corresponding to these masses. The propene mass spectrum has a peak at *m/z* 66 (C_5H_6), which corresponds to isomers of cyclopentadiene; this peak is not apparent in the propyne mass spectrum. The absence of *m/z* 66 for propyne pyrolysis suggests that direct pathways for the formation of C_5H_6 species, such as allyl + acetylene [56] and propargyl + acetylene [29,30,81], are not available for propyne pyrolysis at this temperature. The formation of cyclopentadiene has been observed previously for both propyne [69] and propene [49,56] pyrolysis and is linked to the formation of the RSR cyclopentadienyl. The CHRCR mechanism suggests that cyclopentadienyl can catalyze RSR growth [22,30] and hydrocarbon clustering through radical chain reactions [22].

Evidence of the CHRCR mechanism is provided by the sequence of RSR peaks at *m/z* 91, 115, 141, 165, 189, 215, and 239 apparent in the propene mass spectra and, to some extent, in the propyne mass spectra, examples of which are shown in Fig. 8. This series of RSRs was previously observed by Johansson et al. [22] in samples extracted from sooting flames and was used to develop the CHRCR hypothesis. The RSR peaks at *m/z* 91 (C_7H_7) and 115 (C_9H_7) are not initially observed for propyne, which indicates that acetylene addition to cyclopentadienyl is not the primary pathway for RSR growth under these conditions.

Prominent peaks corresponding to C_6 products are apparent at *m/z* 78 (C_6H_6) and 80 (C_6H_8) for both reactants. The self-reaction of propargyl radicals is well known to produce the C_6H_6 isomers benzene and fulvene at low pressures [42,93]; 1,5-hexadiyne and 2-ethynyl-1,3-butadiene have also been observed at low pressures (27–40 kPa, 200–300 Torr) and high temperatures (1300 K) [66]. At elevated temperatures and pressures close to 100 kPa, however, the major products are 1,5-hexadiyne, dimethylenecyclobutene, and benzene [93].

The self-reaction of allyl has been shown to produce 1,5-hexadiene at *m/z* 82 (C_6H_{10}) at temperatures of 300 - 600 K and pressures of 0.1 – 0.8 kPa (1–6 Torr) [94]. Although a peak at this mass is not apparent in our mass spectra for propene or propyne pyrolysis, it is possible that this species does not adsorb to particles strongly enough to be measurable by the VUV-AMS.

The peak at *m/z* 80 (C_6H_8) may be the cyclic product predicted for the reaction of allyl with propargyl (methylcyclopentadiene or cyclohexadiene) [46,72]; this product, however, has been predicted to be less likely to form at elevated pressures [46]. The propene pyrolysis mass spectrum has a peak at *m/z* 65 and suggests the formation of cyclopentadienyl at (C_5H_5), which can react with methyl radical at elevated temperatures to form 5-methylcyclopentadiene [68]; the absence of a peak at *m/z* 65 in Fig. 8b precludes this route to the formation of C_6H_8 for propyne. Alternatively, the C_6H_8 species may be formed through direct dimerization of propyne.

The last sets of peaks in the C_5–C_9 subset include *m/z* 105, 115/116, and 118/119. The peak at *m/z* 105 is apparent for both reactants. For propyne, a pathway to this mass could be through acetylene addition to *m/z* 80 isomers, such as methylcyclopentadiene [95]. For propene, additional plausible pathways to *m/z* 105 include methyl addition to *m/z* 91 or propargyl addition to cyclopentadiene [96]. Pathways to C_9 masses are limited and include acetylene addition to vinyl-cyclopentadienyl, yielding *m/z* 116 in propene pyrolysis, and propargyl addition to *m/z* 80 isomers, yielding *m/z* 119 in propyne pyrolysis, as shown in Scheme 2. The absence of *m/z* 116 in the propyne mass spectrum at particle onset suggests that propargyl addition to phenyl is not the dominant pathway for the formation of C_9 species in propyne pyrolysis, despite previous work suggesting the importance of this reaction to indene formation [52]. Within 50 K after particle onset, *m/z* 91 and

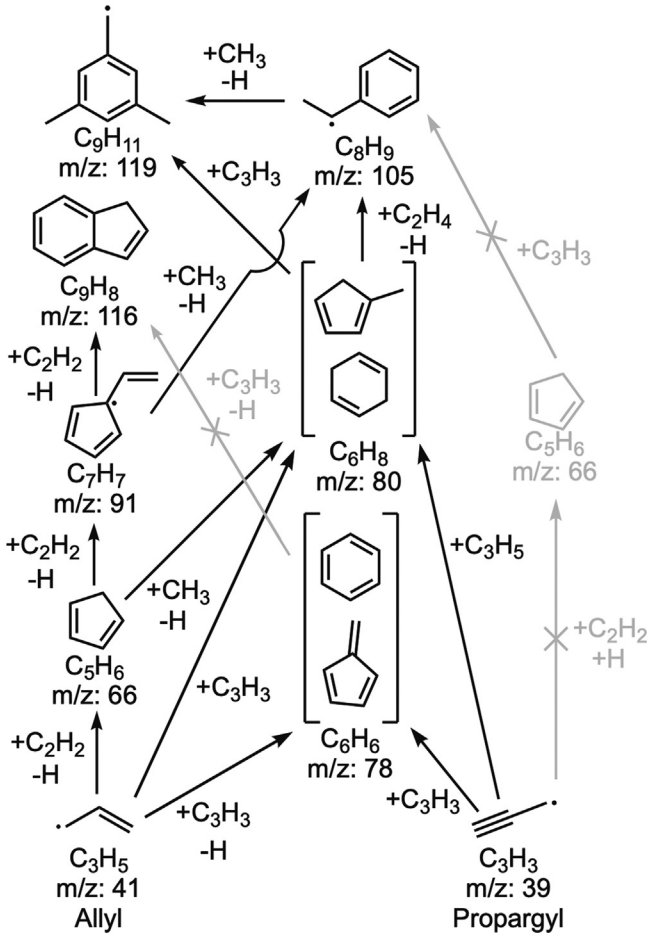

Scheme 2. Simplified depiction of initial growth pathways leading to masses apparent in the VUV-AMS mass spectra. Reaction schemes start with the RSR products of hydrogen loss from propene (bottom left) and propyne (bottom right). Gray arrows indicate pathways that lead to stable intermediates with masses not observed in the mass spectra. The species shown are speculative and do not necessarily represent the isomers observed.

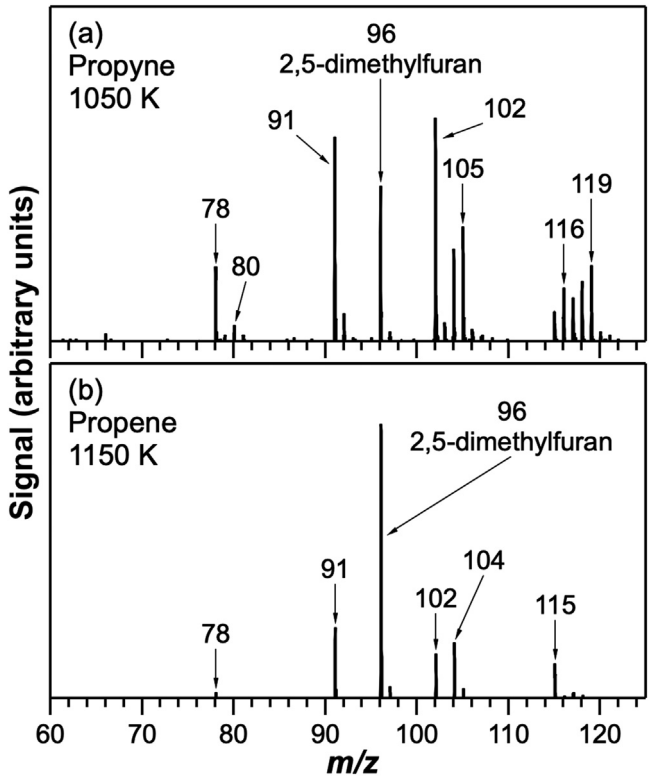

Fig. 9. VUV-AMS mass spectra at 50 K above the particle onset temperature. Mass spectra are shown for (a) propyne at 1050 K and (b) propene at 1150 K over the mass range of *m/z* 60–125. The VUV-AMS mass spectra were recorded at a photon energy of 9.5 eV.

116 both emerge in the mass spectrum for propyne, which can be seen in Fig. 9a. The concurrent emergence of *m/z* 91 and 116 supports the pathway to indene formation through acetylene addition to vinyl-cyclopentadienyl [22] and discounts the route of propargyl addition to phenyl. For propene pyrolysis at 1150 K, shown in Fig. 9b, peaks *m/z* 66 and 80 are not apparent in the mass spectrum, but the peak at *m/z* 91 is still present. This result suggests that additional pathways involving masses that are not observed in the VUV-AMS mass spectra, such as C_3 and C_4 species, also contribute to the formation of products at *m/z* 91.

The C_9 species appear to be involved in the formation of larger species. Previous work identified the reaction of the RSR indenyl with indenyl/indene, which leads to *m/z* 230 ($C_{18}H_{14}$), as an important clustering pathway in indene pyrolysis [32,35]. At the particle onset temperatures, the mass spectrum for propene shows a peak at *m/z* 116, associated with indene (Fig. 8a), and a higher relative intensity for *m/z* 230 than demonstrated in the propyne mass spectrum (Fig. 8b), which shows a peak at *m/z* 119 instead of *m/z* 116. The presence of *m/z* 116 and higher relative intensity of *m/z* 230 in the VUV-AMS mass spectrum for propene indicates that, close to the particle-onset temperature, the presence of *m/z* 116 and 230 are linked, providing further support for the previous identification of the indenyl self-reaction as a potential clustering pathway. The peak at *m/z* 119 in the propyne mass spectrum (Fig. 8b), on the other hand, does not appear to be directly linked to *m/z* 230 or the C_{18} series.

3.4. Photoionization efficiency curves

Mass-specific PIE curves can provide additional insight into the underlying chemistry of a system by supplying information about the isomeric composition of a given mass peak. Fig. 10 shows PIE curves for selected masses observed in the VUV-AMS data for both propyne and propene. The curves were recorded at a reactor temperature of 1225 K, and the signals were consistent over multiple experimental trials. The masses shown in Fig. 10 correspond to $C_{10}H_8$, $C_{11}H_{10}$, $C_{12}H_8$, $C_{13}H_{10}$, $C_{14}H_{10}$, $C_{15}H_{12}$, $C_{18}H_{14}$, and $C_{20}H_{12}$ species. For the species between and including *m/z* 128 ($C_{10}H_8$) and 152 ($C_{12}H_8$), the PIE curves for propyne and propene are very similar. For the masses larger than *m/z* 152, however, the PIE curves for the two reactants demonstrate differences from one another. These differences are apparent for both the odd- and even-numbered carbon species. Reaction intermediates are thus similar for propyne and propene pyrolysis for species up to approximately the size of acenaphthylene ($C_{12}H_8$). The PIE curves suggest differences between the reactants for larger species and the associated kinetics related to further PAH growth.

The definitive identification of a specific isomeric structure for PAHs with more than roughly 10 carbons is often precluded by a large number of possible isomers with similar ionization energies and the lack of known ionization energies or reference curves available for most of these isomers [77,97]. Nevertheless, comparisons can be made between experimental PIE curves and ionization energies, when available, to rule out the involvement of some isomers or provide some indication of the involvement of selected isomers or classes of isomeric structures [77,97].

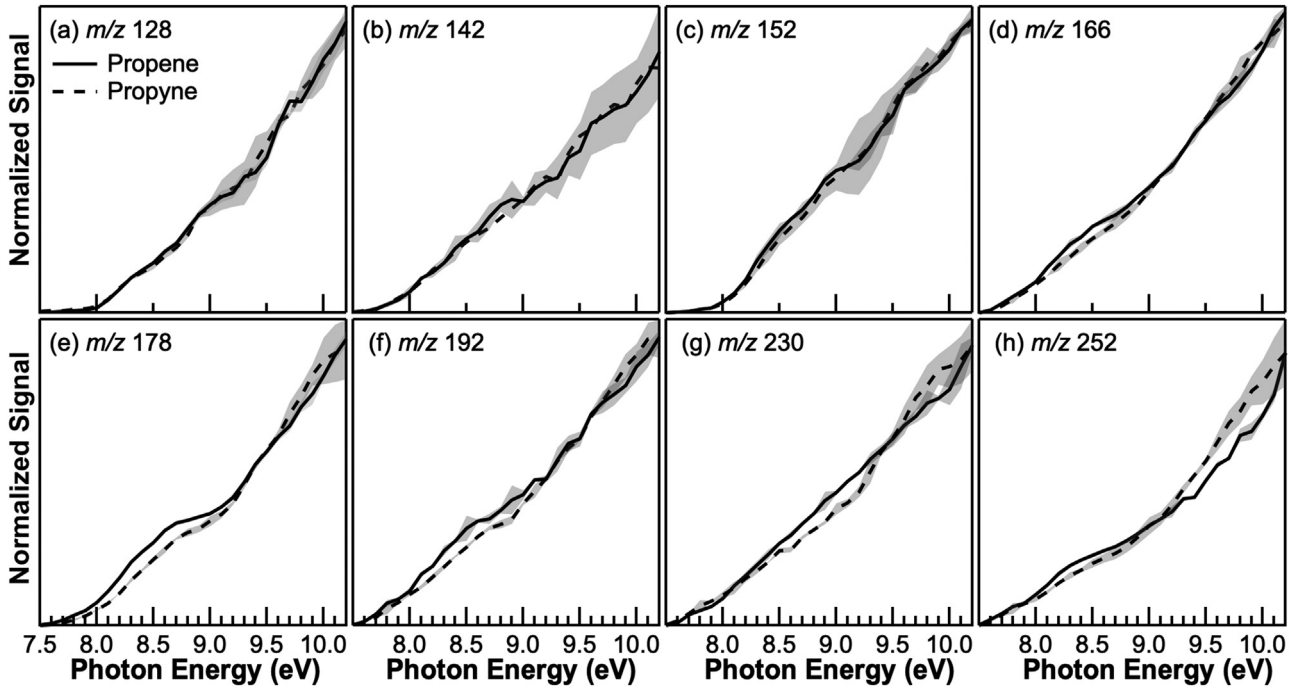

Fig. 10. Normalized photoionization efficiency (PIE) curves from VUV-AMS data. PIE curves are shown for selected mass peaks resulting from propyne pyrolysis and propene pyrolysis at 1225 K. Masses correspond to species with compositions of (a) $C_{10}H_8$, (b) $C_{11}H_{10}$, (c) $C_{12}H_8$, (d) $C_{13}H_{10}$, (e) $C_{14}H_{10}$, (f) $C_{15}H_{12}$, (g) $C_{18}H_{14}$, and (h) $C_{20}H_{12}$. Error bars (shading) represent a 95% confidence interval.

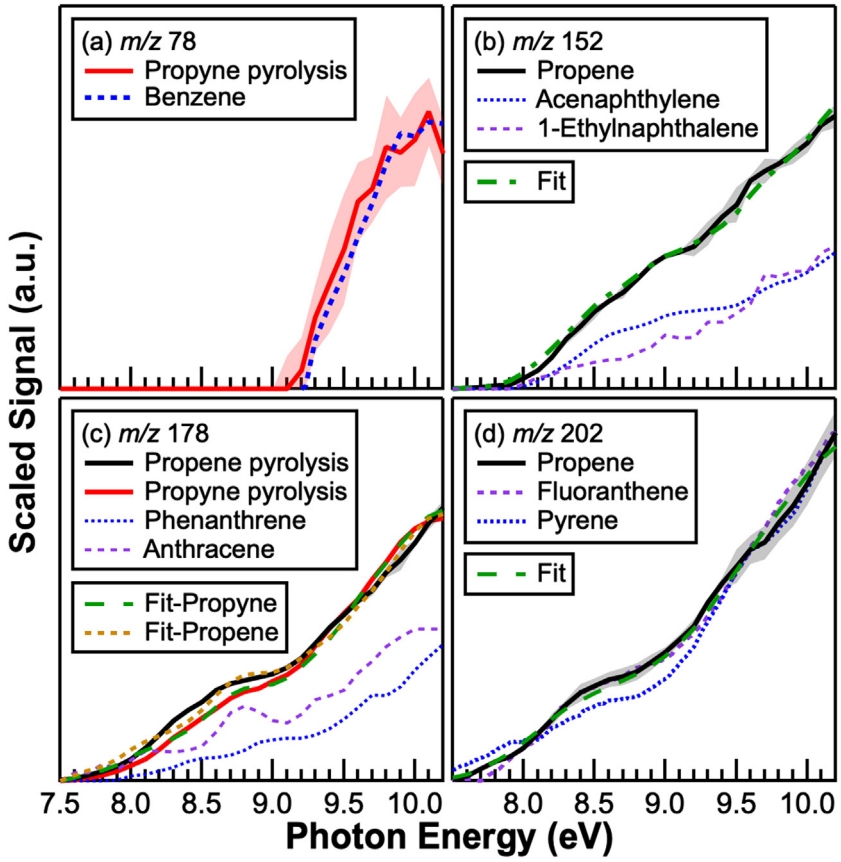

Fig. 11. Normalized PIE curves from VUV-AMS data compared with reference PIE curves from the literature. PIE curves are shown for selected mass peaks resulting from propyne pyrolysis and propene pyrolysis at 1225 K, including (a) *m/z* 78 (C_6H_6), (b) *m/z* 152 ($C_{12}H_8$), (c) *m/z* 178 ($C_{14}H_{10}$), (d) *m/z* 202 ($C_{16}H_{10}$). Reference curves shown are reproduced from (a) [98] for benzene, (b) [99] for acenaphthylene and 1-ethylnaphthalene, (c) [100] for phenanthrene and anthracene, and (d) [97] for fluoranthene and pyrene. Error bars (shading) represent a 95% confidence interval.

Fig. 11 shows comparisons between our experimental PIE curves for selected masses and reference PIE curves from the literature [97–100]. In Fig. 11, reference PIE curves were scaled relative to their absolute photoionization cross-sections and, for each respective *m/z*, retain their relative relationship to one another. Fig. 11a shows that *m/z* 78 from propyne pyrolysis agrees well with the reference PIE curve for benzene, suggesting that benzene is the major product of propargyl self-reaction under these conditions. The mass peak at *m/z* 78 is not apparent for propene pyrolysis at the temperature of 1225 K at which the PIE curves were recorded. For *m/z* 152, the experimental PIE curve for propene pyrolysis was reproduced by a fit based on a combination of approximately 60% acenaphthylene and 40% 1-ethylnaphthalene PIE curves, as shown in Fig. 11b. Fig. 11c demonstrates that a combination of approximately 35% anthracene and 65% phenanthrene reproduces the PIE curve for *m/z* 178 from propyne pyrolysis. A combination of these curves does not provide a good fit to the data from propene pyrolysis, and the inclusion of the *m/z* 178 isomer diphenylacetylene does not improve the fit for either reactant. Anthracene is the stabilomer for $C_{14}H_{10}$ (*m/z* 178) [73], and these results again demonstrate that the stabilomer species is not the only, or even the major, species at this mass. Fig. 11d shows comparisons of experimental results for *m/z* 202 with a fit combining approximately 90% fluoranthene and 10% pyrene. These results are consistent with previous work indicating that fluoranthene is the major contributor to experimental signals from combustion and pyrolysis of hydrocarbon fuels and that pyrene contributes much less significantly to this mass peak [35,67,74-77].

4. Conclusions

In this work, we conducted pyrolysis experiments on propyne and propene in an atmospheric pressure flow reactor and analyzed the products using VUV-AMS. The particle-onset temperature in propyne pyrolysis is approximately 100 K below the onset temperature for propene. The VUV-AMS mass spectra showed a significant range of peaks with high levels of saturation for a given number of carbons (particularly in peak sets larger than C_{17}) at temperatures within 100 K of the onset temperature. The C/H ratio is significantly lower than those of stabilomer species and peri–condensed PAHs, particularly for species larger than C_{17}. The differences in saturation between the pyrolysis products and the stabilomer PAHs are largest in the low-temperature regime. The high saturation levels, particularly for large species, is not well explained by sequential mass growth as traditionally predicted by the HACA mechanism; these results suggest that large species with high levels of saturation are produced through clustering-type reactions, as predicted by the CHRCR mechanism.

Two masses previously linked to RSRs, *m/z* 91 and 115, are produced in propene pyrolysis but not observed for propyne pyrolysis. At the particle-onset temperature, different peaks are associated with the C_9 peak series; in propene pyrolysis, species with *m/z* 116 are generated, and, in propyne pyrolysis, species with *m/z* 119 are produced. The *m/z* 116 peak in propene pyrolysis is linked to indenyl and the formation of a dimer at *m/z* 230, whereas the *m/z* 119 peak from propyne pyrolysis is not obviously linked to the formation of any larger masses. PIE curves indicate that, at 1225 K, PAH formation follows a common set of pathways and products for masses less than approximately *m/z* 152 ($C_{12}H_8$) for the two reactants. For masses above *m/z* 152, differences between the PIE curves for propene and propyne pyrolysis indicate different isomeric profiles between the two reactants and suggest diverging kinetic pathways in the formation of larger PAHs.

Declaration of Competing Interest

The authors declare that they have no known competing financial interests or personal relationships that could have appeared to influence the work reported in this paper.

Acknowledgments

HAM, KOJ, PES, JZ, and KRW were supported by the Gas Phase Chemical Physics Program in the Chemical Sciences, Geosciences, and Biosciences Division of the Office of Basic Energy Sciences of the U.S. Department of Energy (DOE). KRW was supported under Contract No. DE-AC02-05CH11231. JZ was supported by FWP 22-022187, and JAR and HAM were supported under a sub-contract from Sandia National Laboratories on FWP 22-022187. RPB was supported by the Sandia Laboratory Directed Research and Development (LDRD) Program. This research used resources of the Advanced Light Source, which is a DOE Office of Science User Facility under contract no. DE-AC02-05CH11231. Sandia National Laboratories is a multi-mission laboratory managed and operated by National Technology & Engineering Solutions of Sandia, LLC, a wholly owned subsidiary of Honeywell International Inc., for the DOE's National Nuclear Security Administration under contract DE-NA0003525. The views expressed in the article do not necessarily represent the views of the DOE or the United States Government.

References

[1] T.C. Bond, S.J. Doherty, D.W. Fahey, P.M. Forster, T. Berntsen, B.J. DeAngelo, M.G. Flanner, S. Ghan, B. Kärcher, D. Koch, S. Kinne, Y. Kondo, P.K. Quinn, M.C. Sarofim, M.G. Schultz, M. Schulz, C. Venkataraman, H. Zhang, S. Zhang, N. Bellouin, S.K. Guttikunda, P.K. Hopke, M.Z. Jacobson, J.W. Kaiser, Z. Klimont, U. Lohmann, J.P. Schwarz, D. Shindell, T. Storelvmo, S.G. Warren, C.S. Zender, Bounding the role of black carbon in the climate system: a scientific assessment, J. Geophys. Res. 118 (2013) 5380–5552.
[2] W.A. Thorsen, W.G. Cope, D. Shea, Bioavailability of PAHs: effects of soot carbon and PAH source, Environ. Sci. Technol. 38 (2004) 2029–2037.
[3] U.S. EPA, 126 Priority Pollutants, Appendix A to Part 423, Title 40, Code of Federal Regulations (2022).
[4] G.M. Solomon, S. Hurley, C. Carpenter, T.M. Young, P. English, P. Reynolds, Fire and water: assessing drinking water contamination after a major wildfire, Environ. Sci. Technol. 1 (2021) 1878–1886.
[5] N.A. Janssen, G. Hoek, M. Simic-Lawson, P. Fischer, L. van Bree, H. ten Brink, M. Keuken, R.W. Atkinson, H.R. Anderson, B. Brunekreef, F.R. Cassee, Black carbon as an additional indicator of the adverse health effects of airborne particles compared with PM10 and PM2.5, Environ. Health Perspect. 119 (2011) 1691–1699.
[6] R.D. Peng, M.L. Bell, A.S. Geyh, A. McDermott, S.L. Zeger, J.M. Samet, F. Dominici, Emergency admissions for cardiovascular and respiratory diseases and the chemical composition of fine particle air pollution, Environ. Health Perspect. 117 (2009) 957–963.
[7] M.Z. Jacobson, Short-term effects of controlling fossil-fuel soot, biofuel soot and gases, and methane on climate, Arctic ice, and air pollution health, J. Geophys. Res. 115 (2010).
[8] A.M. Nienow, J.T. Roberts, Heterogeneous chemistry of carbon aerosols, Annu. Rev. Phys. Chem. 57 (2006) 105–128.
[9] M. Shiraiwa, K. Selzle, U. Poschl, Hazardous components and health effects of atmospheric aerosol particles: reactive oxygen species, soot, polycyclic aromatic compounds and allergenic proteins, Free Radic. Res. 46 (2012) 927–939.
[10] IPCC, Climate ChangeThe Physical Science Basis. Working Group I Contribution to the Fifth Assessment Report of the Intergovernmental Panel On Climate Change 2013, Cambridge University Press, Cambridge, UK and New York, NY, 2013.
[11] L.G. Jahl, T.A. Brubaker, M.J. Polen, L.G. Jahn, K.P. Cain, B.B. Bowers, W.D. Fahy, S. Graves, R.C. Sullivan, Atmospheric aging enhances the ice nucleation ability of biomass-burning aerosol, Sci. Adv. 7 (2021) eabd3440.
[12] B. Guan, R. Zhan, H. Lin, Z. Huang, Review of the state-of-the-art of exhaust particulate filter technology in internal combustion engines, J. Environ. Manage. 154 (2015) 225–258.
[13] F. Caiazzo, A. Ashok, I.A. Waitz, S.H.L. Yim, S.R.H. Barrett, Air pollution and early deaths in the United States. Part I: quantifying the impact of major sectors in 2005, Atmos. Environ. 79 (2013) 198–208.
[14] M. Monthioux, H. Allouche, R.L. Jacobsen, Chemical vapor deposition of pyrolytic carbon on carbon nanotubes Part 3: growth mechanisms, Carbon 44 (2006) 3183–3194.
[15] I.C. Lewis, L.S. Singer, Electron spin resonance of stable aromatic radical intermediates in pyrolysis, Carbon 7 (1969) 95–99.

[16] J.R. Prekodravac, D.P. Kepic, J.C. Colmenars, D.A. Giannakoudakis, S.P. Jovanovic, A comprehensive review on selected graphene synthesis methods: from electrochemical exfoliation through rapid thermal annealing towards biomass pyrolysis, J. Mater. Chem. C 9 (2021) 6722–6748.
[17] B.S. Haynes, H.G. Wagner, Soot formation, Prog. Energy Combust. Sci. 7 (1981) 229–273.
[18] H.G. Wagner, Soot formation in combustion, Symp. (Int.) Combust. 17 (1979) 3–19.
[19] K.H. Homann, H.G. Wagner, Some new aspects of the mechanism of carbon formation in premixed flames, Symp. (Int.) Combust. 11 (1967) 371–379.
[20] H. Wang, M. Frenklach, A detailed kinetic modeling study of aromatics formation in laminar premixed acetylene and ethylene flames, Combust. Flame 110 (1997) 173–221.
[21] H.A. Michelsen, M.B. Colket, P.-.E. Bengtsson, A. D'Anna, P. Desgroux, B.S. Haynes, J.H. Miller, G.J. Nathan, H. Pitsch, H. Wang, A review of terminology used to describe soot formation and evolution under combustion and pyrolytic conditions, ACS Nano 14 (2020) 12470–12490.
[22] K.O. Johansson, M.P. Head-Gordon, P.E. Schrader, K.R. Wilson, H.A. Michelsen, Resonance-stabilized hydrocarbon-radical chain reactions may explain soot inception and growth, Science 361 (2018) 997–1000.
[23] L.G. Blevins, R.A. Fletcher, W.H. Benner, E.B. Steele Jr, G.W. Mulholland, The existence of young soot in the exhaust of inverse diffusion flames, Proc. Combust. Inst. 29 (2002) 2325–2333.
[24] R.A. Dobbins, R.A. Fletcher, H.-.C. Chang, The evolution of soot precursor particles in a diffusion flame, Combust. Flame 115 (1998) 285–298.
[25] K.H. Homann, Fullerenes and soot formation—New pathways to large particles in flames, Angew. Chem. Int. Ed. Engl. 37 (1998) 2434–2451.
[26] B. Öktem, M.P. Tolocka, B. Zhao, H. Wang, M.V. Johnston, Chemical species associated with the early stage of soot growth in a laminar premixed ethylene-oxygen-argon flame, Combust. Flame 142 (2005) 364–373.
[27] S.A. Skeen, H.A. Michelsen, K.R. Wilson, D.M. Popolan, A. Violi, N. Hansen, Near-threshold photoionization mass spectra of combustion-generated high–molecular-weight soot precursors, J. Aerosol Sci. 58 (2013) 86–102.
[28] P. Desgroux, A. Faccinetto, X. Mercier, T. Mouton, D. Aubagnac Karkar, E. Bakali, Comparative study of the soot formation process in a "nucleation" and a "sooting" low pressure premixed methane flame, Combust. Flame 184 (2017) 153–166.
[29] V.D. Knyazev, I.R. Slagle, Kinetics of the reaction between propargyl radical and acetylene, J. Phys. Chem. A 106 (2002) 5613–5617.
[30] J.D. Savee, T.M. Selby, O. Welz, C.A. Taatjes, D.L. Osborn, Time- and isomer-resolved measurements of sequential addition of acetylene to the propargyl radical, Journal of Physical Chemistry Letters 6 (2015) 4153–4158.
[31] H. Jin, L. Xing, J. Hao, J. Yang, Y. Zhang, C. Cao, Y. Pan, A. Farooq, A chemical kinetic modeling study of indene pyrolysis, Combust. Flame 206 (2019) 1–20.
[32] H. Jin, J. Yang, L. Xing, J. Hao, Y. Zhang, C. Cao, Y. Pan, A. Farooq, An experimental study of indene pyrolysis with synchrotron vacuum ultraviolet photoionization mass spectrometry, Phys. Chem. Chem. Phys. 21 (2019) 5510–5520.
[33] H. Jin, L. Xing, D. Liu, J. Hao, J. Yang, A. Farooq, First aromatic ring formation by the radical-chain reaction of vinylacetylene and propargyl, Combust. Flame 225 (2021) 524–534.
[34] D.E. Couch, A.J. Zhang, C.A. Taatjes, N. Hansen, Experimental observation of hydrocarbon growth by resonance-stabilized radical-radical chain reaction, Angew. Chem. Int. Ed. Engl. 60 (2021) 27230–27235.
[35] J.A. Rundel, C.M. Thomas, P.E. Schrader, K.R. Wilson, K.O. Johansson, R.P. Bambha, H.A. Michelsen, Promotion of particle formation by resonance-stabilized radicals during hydrocarbon pyrolysis, Combust. Flame (2021) 111942, doi:10.1016/j.combustflame.2021.111942.
[36] S.G. Davis, C.K. Law, H. Wang, An experimental and kinetic modeling study of propyne oxidation, Twenty Seventh Symp. (Int.) Combust. 27 (1998) 305–312.
[37] A. Chakir, M. Cathonnet, J.C. Boettner, F. Gaillard, Kinetic study of n-butane oxidation, Combust. Sci. Technol. 65 (1989) 207–230.
[38] P. Dagaut, M. Cathonnet, J. Boettner, Experimental study and kinetic modeling of propene oxidation in a jet stirred flow reactor, J. Phys. Chem. 92 (1988) 661–671.
[39] S.E. Wheeler, K.A. Robertson, W.D. Allen, Y. Schaefer, J. Bomble, J.F. Stanton, Thermochemistry of key soot formation intermediates: C_3H_3 isomers, J. Phys. Chem. A 111 (2007) 3819–3830.
[40] J.A. Miller, S.J. Klippenstein, From the multiple-well master equation to phenomenological rate coefficients: reactions on a C_3H_4 potential energy surface, J. Phys. Chem. A 107 (2003) 2680–2692.
[41] L. Ye, Y. Georgievskii, S.J. Klippenstein, Pressure-dependent branching in the reaction of $^1CH_2$ with C_2H_4 and other reactions on the C_3H_6 potential energy surface, Proc. Combust. Inst. 35 (2015) 223–230.
[42] J.A. Miller, S.J. Klippenstein, The Recombination of Propargyl Radicals and Other Reactions on a C6H6 Potential, J. Phys. Chem. A 107 (2003) 7783–7799.
[43] S.E. Stein, J.A. Walker, M.M. Suryan, A. Fahr, A new path to benzene in flames, Symp. (Int.) Combust. 23 (1991) 85–90.
[44] C.S. McEnally, L.D. Pfefferle, B. Atakan, K. Kohse-Höinghaus, Studies of aromatic hydrocarbon formation mechanisms in flames: progress towards closing the fuel gap, Prog. Energy Combust. Sci. 32 (2006) 247–294.
[45] H. Richter, J.B. Howard, Formation of polycyclic aromatic hydrocarbons and their growth to soot—A review of chemical reaction pathways, Prog. Energy Combust. Sci. 26 (2000) 565–608.
[46] J.A. Miller, S.J. Klippenstein, Y. Georgievskii, L.B. Harding, W.D. Allen, A.C. Simmonett, Reactions between resonance-stabilized radicals: propargyl+ allyl, J. Phys. Chem. A 114 (2010) 4881–4890.
[47] Y. Hidaka, T. Nakamura, A. Miyauchi, T. Shiraishi, H. Kawano, Thermal decomposition of propyne and allene in shock waves, Int. J. Chem. Kinet. 21 (1989) 643–666.
[48] N. Hansen, J.A. Miller, P.R. Westmoreland, T. Kasper, K. Kohse-Höinghaus, J. Wang, T.A. Cool, Isomer-specific combustion chemistry in allene and propyne flames, Combust. Flame 156 (2009) 2153–2164.
[49] S.G. Davis, C.K. Law, H. Wang, Propene pyrolysis and oxidation kinetics in a flow reactor and laminar flames, Combust. Flame 119 (1999) 375–399.
[50] P. Barbé, R. Martin, D. Perrin, G. Scacchi, Kinetics and modeling of the thermal reaction of propene at 800K. Part I. Pure propene, Int. J. Chem. Kinet. 28 (1996) 829–847.
[51] Y. Hidaka, T. Nakamura, H. Tanaka, A. Jinno, H. Kawano, T. Higashihara, Shock tube and modeling study of propene pyrolysis, Int. J. Chem. Kinet. 24 (1992) 761–780.
[52] N. Hansen, B. Yang, M. Braun-Unkhoff, A. Ramirez, G. Kukkadapu, Molecular-growth pathways in premixed flames of benzene and toluene doped with propyne, Combust. Flame (2022) 112075, doi:10.1016/j.combustflame.2022.112075.
[53] W. Sun, A. Hamadi, S. Abid, N. Chaumeix, A. Comandini, A comprehensive kinetic study on the speciation from propylene and propyne pyrolysis in a single-pulse shock tube, Combust. Flame 231 (2021) 111485.
[54] S. Panigrahy, J. Liang, M.K. Ghosh, Q.-.D. Wang, Z. Zuo, S. Nagaraja, A.A.E.-S. Mohamed, G. Kim, S.S. Vasu, H.J. Curran, An experimental and detailed kinetic modeling study of the pyrolysis and oxidation of allene and propyne over a wide range of conditions, Combust. Flame 233 (2021) 111578.
[55] G. Kukkadapu, S.W. Wagnon, W.J. Pitz, N. Hansen, Identification of the molecular-weight growth reaction network in counterflow flames of the C3H4 isomers allene and propyne, Proc. Combust. Inst. 38 (2021) 1477–1485.
[56] K. Wang, S.M. Villano, A.M. Dean, Fundamentally-based kinetic model for propene pyrolysis, Combust. Flame 162 (2015) 4456–4470.
[57] N.B. Poddar, S. Thomas, M.J. Wornat, Polycyclic aromatic hydrocarbons from the co-pyrolysis of 1,3-butadiene and propyne, Proc. Combust. Inst. 34 (2013) 1775–1783.
[58] W. Sun, A. Hamadi, S. Abid, N. Chaumeix, A. Comandini, Influences of propylene/propyne addition on toluene pyrolysis in a single-pulse shock tube, Combust. Flame 236 (2022) 111799.
[59] J. Shu, K.R. Wilson, M. Ahmed, S.R. Leone, Coupling a versatile aerosol apparatus to a synchrotron: vacuum ultraviolet light scattering, photoelectron imaging, and fragment free mass spectrometry, Rev. Sci. Instrum. 77 (2006).
[60] E. Gloaguen, E.R. Mysak, S.R. Leone, M. Ahmed, K.R. Wilson, Investigating the chemical composition of mixed organic–inorganic particles by “soft” vacuum ultraviolet photoionization: the reaction of ozone with anthracene on sodium chloride particles, Int. J. Mass Spectrom. 258 (2006) 74–85.
[61] J.M. Headrick, P.E. Schrader, H.A. Michelsen, Radial-profile and divergence measurements of combustion-generated soot focused by an aerodynamic-lens system, J. Aerosol Sci. 58 (2013) 158–170.
[62] P.S.K. Liu, R. Deng, K.A. Smith, L.R. Williams, J.T. Jayne, M.R. Canagaratna, K. Moore, T.B. Onasch, D.R. Worsnop, T. Deshler, Transmission efficiency of an aerodynamic focusing lens system: comparison of model calculations and laboratory measurements for the aerodyne aerosol mass spectrometer, Aerosol Sci. Technol. 41 (2007) 721–733.
[63] X. Zhang, K.A. Smith, D.R. Worsnop, J.-.L. Jimenez, J.T. Jayne, C.E. Kolb, J. Morris, P. Davidovits, Numerical characterization of particle beam collimation: part II. Integrated aerodynamic-lens-nozzle system, Aerosol Sci. Technol. 38 (2004) 619–638.
[64] WaveMetrics, Igor Pro, Lake Oswego, OR, USA.
[65] M. Xie, Z. Zhou, Z. Wang, D. Chen, F. Qi, Determination of absolute photoionization cross-sections of oxygenated hydrocarbons, Int. J. Mass Spectrom. 293 (2010) 28–33.
[66] L. Zhao, W. Lu, M. Ahmed, M.V. Zagidullin, V.N. Azyazov, A.N. Morozov, A.M. Mebel, R.I. Kaiser, Gas-phase synthesis of benzene via the propargyl radical self-reaction, Sci. Adv. 7 (2021) eabf0360.
[67] S. Sinha, R.K. Rahman, A. Raj, On the role of resonantly stabilized radicals in polycyclic aromatic hydrocarbon (PAH) formation: pyrene and fluoranthene formation from benzyl–indenyl addition, Phys. Chem. Chem. Phys. 19 (2017) 19262–19278.
[68] B.K. Carpenter, G.B. Ellison, M.R. Nimlos, A.M. Scheer, A conical intersection influences the ground state rearrangement of fulvene to benzene, J. Phys. Chem. A 126 (2022) 1429–1447.
[69] S.G. Davis, C.K. Law, H. Wang, Propyne pyrolysis in a flow reactor: an experimental, RRKM, and detailed kinetic modeling study, J. Phys. Chem. A 103 (1999) 5889–5899.
[70] K. Wang, S.M. Villano, A.M. Dean, Reactions of allylic radicals that impact molecular weight growth kinetics, Phys. Chem. Chem. Phys. 17 (2015) 6255–6273.
[71] A. Fridlyand, P.T. Lynch, R.S. Tranter, K. Brezinsky, Single pulse shock tube study of allyl radical recombination, J. Phys. Chem. A 117 (2013) 4762–4776.
[72] A. Matsugi, K. Suma, A. Miyoshi, Kinetics and mechanisms of the Allyl + Allyl and Allyl + propargyl recombination reactions, J. Phys. Chem. A 115 (2011) 7610–7624.
[73] S.E. Stein, A. Fahr, High-temperature stabilities of hydrocarbons, J. Phys. Chem. 89 (1985) 3714–3725.

[74] K.O. Johansson, J.Y.W. Lai, S.A. Skeen, D.M. Popolan-Vaida, K.R. Wilson, N. Hansen, A. Violi, H.A. Michelsen, Soot precursor formation and limitations of the stabilomer grid, Proc. Combust. Inst. 35 (2015) 1819–1826.
[75] T. Mouton, X. Mercier, P. Desgroux, Isomer discrimination of PAHs formed in sooting flames by jet-cooled laser-induced fluorescence: application to the measurement of pyrene and fluoranthene, Appl. Phys. B 122 (2016) 123.
[76] K.O. Johansson, T. Dillstrom, P. Elvati, M.F. Campbell, P.E. Schrader, D.M. Popolan-Vaida, N.K. Richards-Henderson, K.R. Wilson, A. Violi, H.A. Michelsen, Radical–radical reactions, pyrene nucleation, and incipient soot formation in combustion, Proc. Combust. Inst. 36 (2017) 799–806.
[77] K.O. Johansson, J. Zádor, P. Elvati, M.F. Campbell, P.E. Schrader, N.K. Richards-Henderson, K.R. Wilson, A. Violi, H.A. Michelsen, Critical assessment of photoionization efficiency measurements for characterization of soot-precursor species, J. Phys. Chem. A 121 (2017) 4475–4485.
[78] A. D'Anna, A. D'Alessio, P. Minutolo, Spectroscopic and chemical characterization of soot inception processes in premixed laminar flames at atmospheric pressure, in: H. Bockhorn (Ed.), Soot Formation in Combustion: Mechanisms and Models, Springer-Verlag, Berlin (1994), pp. 83–103.
[79] R.A. Dobbins, H. Subramaniasivam, Soot precursors: particles in flames, in: H. Bockhorn (Ed.), Soot Formation in Combustion, Springer-Verlag, Berlin (1994), pp. 290–301.
[80] J.P. Cain, P.L. Gassman, H. Wang, A. Laskin, Micro-FTIR study of soot chemical composition—evidence of aliphatic hydrocarbons on nascent soot surfaces, Phys. Chem. Chem. Phys. 12 (2010) 5206–5218.
[81] M. Frenklach, Reaction mechanism of soot formation in flames, Phys. Chem. Chem. Phys. 4 (2002) 2028–2037.
[82] M. Commodo, K. Kaiser, G. De Falco, P. Minutolo, F. Schulz, A. D'Anna, L. Gross, On the early stages of soot formation: molecular structure elucidation by high-resolution atomic force microscopy, Combust. Flame 205 (2019) 154–164.
[83] F. Schulz, M. Commodo, K. Kaiser, G. De Falco, P. Minutolo, G. Meyer, A. D'Anna, L. Gross, Insights into incipient soot formation by atomic force microscopy, Proc. Combust. Inst. 37 (2019) 885–892.
[84] A. Nobili, L.P. Maffei, A. Baggioli, M. Pelucchi, A. Cuoci, C. Cavallotti, T. Faravelli, On the radical behavior of large polycyclic aromatic hydrocarbons in soot formation and oxidation, Combust. Flame 235 (2022) 111692.
[85] A. Nobili, A. Cuoci, W. Pejpichestakul, M. Pelucchi, C. Cavallotti, T. Faravelli, Modeling soot particles as stable radicals: a chemical kinetic study on formation and oxidation. Part 1. Soot formation in ethylene laminar premixed and counterflow diffusion flames, Combust. Flame (2022) in press, doi:10.1016/j.combustflame.2022.112073.
[86] A. Menon, J.W. Martin, G. Leon, D. Hou, L. Pascazio, X. You, M. Kraft, Reactive localized π-radicals on rim-based pentagonal rings: properties and concentration in flames, Proc. Combust. Inst. 38 (2021) 565–573.
[87] S.-H. Chung, A. Violi, Peri-condensed aromatics with aliphatic chains as key intermediates for the nucleation of aromatic hydrocarbons, Proc. Combust. Inst. 33 (2011) 693–700.
[88] A.D. Anna, A. Violi, A. D'Alessio, A.F. Sarofim, A reaction pathway for nanoparticle formation in rich premixed flames, Combust. Flame 127 (2001) 1995–2003.
[89] B.D. Adamson, S.A. Skeen, M. Ahmed, N. Hansen, Detection of aliphatically bridged multi-core polycyclic aromatic hydrocarbons in sooting flames with atmospheric-sampling high-resolution tandem mass spectrometry, J. Phys. Chem. A 122 (2018) 9338–9349.
[90] A. Violi, A. Kubota, T.N. Truong, W.J. Pitz, C.K. Westbrook, A.F. Sarofim, A fully integrated kinetic monte carlo/molecular dynamics approach for the simulation of soot precursor growth, Proc. Combust. Inst. 29 (2002) 2343–2349.
[91] M.F. Campbell, P.E. Schrader, A.L. Catalano, K.O. Johansson, G.A. Bohlin, N.K. Richards-Henderson, C.J. Kliewer, H.A. Michelsen, A small porous-plug burner for studies of combustion chemistry and soot formation, Rev Sci Instrum 88 (2017) 125106.
[92] K.O. Johansson, T. Dillstrom, M. Monti, F. El Gabaly, M.F. Campbell, P.E. Schrader, D.M. Popolan-Vaida, N.K. Richards-Henderson, K.R. Wilson, A. Violi, H.A. Michelsen, Formation and emission of large furans and oxygenated hydrocarbons from flames, Proc. Natl. Acad. Sci. U. S. A. 113 (2016) 8374–8379.
[93] P.-.T. Howe, A. Fahr, Pressure and temperature effects on product channels of the propargyl (HC=CCH2) combination reaction and the formation of the "first ring, J. Phys. Chem. A 107 (2003) 9603–9610.
[94] T.M. Selby, G. Meloni, F. Goulay, S.R. Leone, A. Fahr, C.A. Taatjes, D.L. Osborn, Synchrotron photoionization mass spectrometry measurements of kinetics and product formation in the allyl radical (H_2CCHCH_2) self-reaction, J. Phys. Chem. A 112 (2008) 9366–9373.
[95] S. Gaïl, P. Dagaut, G. Black, J.M. Simmie, Kinetics of 1,2-dimethylbenzene oxidation and ignition: experimental and detailed chemical kinetic modeling, Combust. Sci. Technol. 180 (2008) 1748–1771.
[96] M.R. Djokic, K.M. Van Geem, C. Cavallotti, A. Frassoldati, E. Ranzi, G.B. Marin, An experimental and kinetic modeling study of cyclopentadiene pyrolysis: first growth of polycyclic aromatic hydrocarbons, Combust. Flame 161 (2014) 2739–2751.
[97] K.O. Johansson, M.F. Campbell, P. Elvati, P.E. Schrader, J. Zádor, N.K. Richards-Henderson, K.R. Wilson, A. Violi, H.A. Michelsen, Photoionization efficiencies of five polycyclic aromatic hydrocarbons, J. Phys. Chem. A 121 (2017) 4447–4454.
[98] T.A. Cool, J. Wang, K. Nakajima, C.A. Taatjes, A. McIlroy, Photoionization cross sections for reaction intermediates in hydrocarbon combustion, Int. J. Mass Spectrom. 247 (2005) 18–27.
[99] H. Jin, J. Yang, A. Farooq, Determination of absolute photoionization cross–sections of some aromatic hydrocarbons, Rapid Commun. Mass Spectrom. 34 (2020) e8899.
[100] L. Zhao, R.I. Kaiser, B. Xu, U. Ablikim, M. Ahmed, M.M. Evseev, E.K. Bashkirov, V.N. Azyazov, A.M. Mebel, Low-temperature formation of polycyclic aromatic hydrocarbons in Titan's atmosphere, Nat. Astron. 2 (2018) 973–979.